The C–H bond dissociation energy of furan: Photoelectron spectroscopy of the furanide anion

Kristen M. Vogelhuber, Scott W. Wren, Leonid Sheps,[a] and W. Carl Lineberger[b]
JILA and Department of Chemistry and Biochemistry, University of Colorado, 440 UCB, Boulder, Colorado 80309, USA

(Received 15 November 2010; accepted 6 January 2011; published online 8 February 2011)

Using photoelectron spectroscopy, we interrogate the cyclic furanide anion ($C_4H_3O^-$) to determine the electron affinity and vibrational structure of the neutral furanyl radical and the term energy of its first excited electronic state. We present the 364-nm photoelectron spectrum of the furanide anion and measure the electron affinity of the $\tilde{X}^2A'$ ground state of the α-furanyl radical to be 1.853(4) eV. A Franck–Condon analysis of the well-resolved spectrum allows determination of the harmonic frequencies of three of the most active vibrational modes upon $\tilde{X}^2A' \leftarrow \tilde{X}^1A'$ photodetachment: 855(25), 1064(25), and 1307(40) cm^{-1}. These modes are ring deformation vibrations, consistent with the intuitive picture of furanide anion photodetachment, where the excess electron is strongly localized on the α-carbon atom. In addition, the $\tilde{A}^2A''$ excited state of the α-furanyl radical is observed 0.68(7) eV higher in energy than the $\tilde{X}^2A'$ ground state. Through a thermochemical cycle involving the known gas-phase acidity of furan, the electron affinity of the furanyl radical yields the first experimental determination of the C–H_α bond dissociation energy of furan ($DH_{298}(C_4H_3O–H_\alpha)$): 119.8(2) kcal mol^{-1}. © *2011 American Institute of Physics*. [doi:10.1063/1.3548873]

I. INTRODUCTION

Furan, C_4H_4O, has attracted considerable attention due to its key role in combustion chemistry as well as to some intriguing aspects of its thermochemistry—namely, to its unusually high calculated C–H bond strength.[1–3] Furan is one of the primary structural units of coal;[4,5] consequently, knowledge of its reactivity has the potential to improve current technology of coal combustion.[6] Furan is also an important intermediate in the pyrolysis of biomass,[7–10] where it is generally thought to originate in the breakdown of polysaccharides that make up cell walls.[11–13] Conversion of biomass (and, more specifically, its major components—lignin, cellulose, and hemicellulose[14]) into ethanol or other fuels has recently stimulated strong interest as a potential alternative to petroleum-based energy production.[15–17] However, at present, thermal biomass processing is not commercially viable because it is inefficient and plagued by undesired reaction products,[18] such as polycyclic aromatic hydrocarbons (PAHs).[19–22] Furan chemistry is central to biomass decomposition; thus, understanding its bond-specific reactivity has far-reaching implications for commercial fuel production, the environment, and the energy economy.

Because of its importance in combustion chemistry and biomass pyrolysis, the thermochemistry of furan has been the subject of several experimental and theoretical investigations. Initial studies focused on thermal decomposition of furan in shock tubes,[23–25] flow reactors,[26,27] and via laser pyrolysis.[28] These experiments established that the two primary product channels of unimolecular furan decomposition are (1) CO + $CH_3C{\equiv}CH$ and (2) $CH_2{=}C{=}O$ + $HC{\equiv}CH$.[23–28] More recently, Vasiliou *et al.* used photoionization mass spectrometry and matrix IR spectroscopy to examine the thermal decomposition products of furan.[29] In addition to the products mentioned above, they detected propargyl radicals (CH_2CCH). Benzene, which is known to form from propargyl radicals,[30] and other aromatic species were also observed in the study,[29] demonstrating the role of furan in the chemistry of PAH formation.

Although the primary decomposition products of furan have been characterized, the mechanisms of their formation are not yet fully known. Several computational studies have been aimed at determining the relative energies of chemical bonds in furan to better understand the mechanistic details of furan decomposition.[1,2,31] One possible pathway begins with the loss of a hydrogen atom bonded to the alpha-carbon in the furan ring; i.e., the cleavage of the C–H_α bond. Yet, the first comprehensive theoretical investigation of the unimolecular decomposition channels of furan[31] concluded that cleavage of the C–H_α bond requires too much energy and therefore cannot be the initial step in any of the major decomposition pathways. Since then, multiple high-level calculations [CBS-QB3,[2] CBS-APNO,[2] G3,[2,3] B3LYP,[3] and CASPT2 (Ref. 1)] agree that the C–H_α bond is prohibitively strong, ~121 kcal mol^{-1}. However, this is an unusually high C–H bond dissociation energy (BDE), which makes its experimental verification a particularly valuable contribution. Because there has been no experimental determination of the C–H_α BDE of furan ($DH_{298}(C_4H_3O–H_\alpha)$) until now, current decomposition models are based on the calculated C–H_α BDE and assume that pathways involving cleavage of the C–H_α bond or H abstraction are unimportant.

[a]Present address: Combustion Research Facility, P.O. Box 969, Mail Stop 9055, Sandia National Laboratories, Livermore, California 94551, USA.
[b]Author to whom correspondence should be addressed. Electronic mail: wcl@jila.colorado.edu.

The C–H_α BDE of furan can be determined through the well-established methodology of a thermochemical cycle[32] involving the electron affinity (EA) of the α-furanyl radical (α-C_4H_3O), the gas-phase acidity of furan, and the ionization energy of hydrogen. The latter quantity is well-known.[33] Likewise, in 1988, DePuy *et al.* investigated the gas-phase acidities of the two distinct hydrogen atoms in furan.[34] As in our experiment, they prepared furanide in a flowing afterglow apparatus by deprotonation of furan with OH^-, and they reported H^+ loss from both the α- and β-positions. They showed that the α-position was the more acidic of the two, but the exact acidity of the β-position was not determined. Calculations and our own observations confirm the higher relative acidity of the α-site, since under our experimental conditions we only observe photodetachment from the α-furanide species. A more precise measurement of the gas-phase acidity of furan was subsequently made by Grabowski and Owusu.[35] In the present work we determine the remaining thermodynamic quantity necessary to obtain the C–H_α BDE of furan: the EA of the α-furanyl radical.

We report a photoelectron spectroscopy study of the furanide anion, which provides several new spectroscopic constants and allows the first direct measurement of the C–H_α BDE of furan. We collect the 364-nm negative ion photoelectron spectrum of $C_4H_3O^-$. From the spectrum, we make the first experimental determination of the EA and of several vibrational frequencies of α-C_4H_3O. We observe both the $\tilde{X}^2A'$ σ-radical ground state and $\tilde{A}^2A''$ π-radical excited state of α-C_4H_3O and determine the term energy (T_e) of the excited state.

II. EXPERIMENTAL METHODS

The negative ion photoelectron spectrometer used in this experiment has been described in detail elsewhere.[36–38] The apparatus consists of four main sections: an ion source, a mass filter, an interaction region with crossed laser and ion beams, and an electrostatic electron kinetic energy analyzer. Negative ions are formed in a flowing afterglow ion source. A microwave discharge containing trace amounts of O_2 gas in He buffer gas (~0.4 Torr) generates atomic oxygen radical anion, O^-. Methane is added downstream of O^- to form hydroxide anion (OH^-), which then reacts with furan (C_4H_4O, ≥99%, Sigma-Aldrich) to generate furanide anions: $OH^- + C_4H_4O \rightarrow C_4H_3O^- + H_2O$. Because the H_α of furan is more acidic,[34] we deprotonate predominantly at the α-position under our experimental conditions to produce the α-furanide anion. We confirm the absence of β-furanide using experimental observations in conjunction with theoretical simulations (see Sec. IV A 3). We do not generate $C_4H_2O^-$; the *m*/*z* 66 peak is absent from our mass spectrum, and it has been shown that $C_4H_2O^-$ is not produced efficiently in the reaction of O^- with furan.[39] Collisions with He buffer gas cool the ions to ~300 K. The flow tube can be further cooled with a liquid nitrogen jacket to obtain a "cold spectrum" of ions with temperatures near 150 K. Anions are extracted into a differentially pumped region and are accelerated to 735 eV before entering a Wien velocity filter with a mass resolution of $m/\Delta m \sim 60$. The mass-selected ion beam (typically 200 pA) is decelerated to 35 eV and focused into the laser interaction region. Here, the 1 W output from a single-mode continuous-wave argon ion laser operating at 364 nm (3.40814 eV) is built up to ~100 W of circulating power in an optical buildup cavity located within the vacuum system. Photoelectrons ejected in the direction orthogonal to both the laser and ion beams enter a hemispherical energy analyzer. The photoelectron signal is recorded as a function of electron kinetic energy with a position-sensitive detector. The energy analyzer has a resolution of ~11 meV under the conditions used for the present experiments.

The electron kinetic energy (eKE) can be converted to electron binding energy (eBE) through the relationship eBE = $h\nu$ − eKE. The absolute kinetic energy scale is calibrated[36,40] before and after each experiment using the well-known EA of atomic oxygen.[41] Additionally, the energy scale is corrected for a slight linear compression (<1%) (Ref. 36) using the photoelectron spectrum of O_2^-, which provides a number of known transitions spanning the photoelectron energy range.[42,43] After making these corrections and accounting for the resolution of the spectrometer and rotational peak profiles, absolute electron binding energies can be determined with an accuracy of better than 5 meV.

A rotatable half-wave plate positioned outside the buildup cavity varies the polarization of the photodetachment radiation in order to control the angle θ between the electric field vector of the laser beam and the photoelectron collection axis. The photoelectron angular distribution is described by the following equation:[44]

$$I(\theta) = \frac{\sigma_0}{4\pi}(1 + \beta P_2(\cos\theta)), \quad (1)$$

where σ_0 is the total photodetachment cross section, β is the anisotropy parameter, and $P_2(\cos\theta)$ is the second Legendre polynomial. We measure the anisotropy parameter explicitly by recording the photoelectron signal at the kinetic energy of one suitable intense peak in the photoelectron spectrum as a function of θ (between $\theta = 0°$ and 360° in steps of 10°). The photoelectron angular distribution is fit with Eq. (1), and full spectra collected at $\theta = 0°$ and 90° are scaled to match β at the energy at which it was measured. Separately, we collect a photoelectron spectrum at $\theta = 54.7°$ (the so-called magic angle), where the photoelectron intensity is independent of β and directly reflects the relative photodetachment cross section.

III. THEORETICAL METHODS

All electronic structure calculations were performed using the GAUSSIAN 03 program package.[45] Optimized geometries, harmonic vibrational frequencies, and normal mode coordinates were calculated at the B3LYP/6–311++G(d,p) level of theory/basis[46] for the $\tilde{X}^1A'$ state of both the α- and β-furanide anions, as well as for the $\tilde{X}^2A'$ and $\tilde{A}^2A''$ states of the neutral α- and β-furanyl radicals. All molecules were constrained to C_s symmetry.

We use a Franck–Condon analysis of the vibrational structure in the furanide photoelectron spectrum to identify the active vibrational modes of the furanyl radical and the

geometry change upon photodetachment. The Franck–Condon profiles of the photoelectron spectra are simulated using the PESCAL program,[43] using as a point of departure the calculated geometries, normal mode vectors, and vibrational frequencies of the anion and neutral states. The normal modes and the Duschinsky $\mathbf{J}''$ matrix and $\mathbf{K}''$ displacements are calculated. The Franck–Condon factors are computed in the harmonic oscillator approximation including Duschinsky rotation using the Sharp–Rosenstock–Chen method.[47] The individual vibronic peak contours are simulated by a Gaussian function with a FWHM of 11 meV, consistent with instrumental resolution. Comparison of the simulations to the experimental spectra enables the determination of experimental frequencies.

IV. RESULTS

A. Photoelectron spectra of the furanide anion

Chemical intuition suggests that the rigid five-membered ring structure constrains furanide to a relatively small geometry change upon photodetachment. Thus, we expect substantial Franck–Condon overlap near the bottom of the $\tilde{X}^2A'$ potential well, making the determination of the origin—and hence the EA—straightforward. We also expect the most significant changes in the geometry of α-furanide upon photodetachment to be localized near the site from which the electron is removed; therefore, we anticipate the active vibrational modes in the photoelectron spectrum to be limited to only a few normal modes involving changes in the bond lengths and angles surrounding the deprotonated C_α.

This simple picture is supported by the well-resolved nature of the photoelectron spectrum we observe. The 364-nm, magic angle, cold (about 150 K) photoelectron spectrum of $C_4H_3O^-$ is presented in Fig. 1(a). We assign the intense, sharp peak at the lowest eBE to the transition from the ground vibrational state of α-furanide to the ground vibrational state of $\tilde{X}^2A'$ α-furanyl radical. The eBE of this origin peak, 1.853(4) eV, directly corresponds to the EA of furanyl radical (Table I). The photoelectron spectrum is dominated by only a few active vibrational modes. From the spectrum we can directly extract three vibrational frequencies of the furanyl radical: 855(25), 1064(25), and 1307(40) cm^{-1}. These frequencies are typical of in-plane ring-distortion and ring-breathing modes.

The photoelectron spectra of $C_4H_3O^-$ collected at 300 K with the laser polarization set at 90° and 0° relative to the direction of photoelectron collection are displayed in Fig. 1(c). In these spectra, a hot band resulting from photodetachment of vibrationally excited anions is visible at lower binding energy than the origin peak. Comparison of the $\theta = 0°$ and $\theta = 90°$ spectra reveals two distinct spectral regions with different anisotropies. Specifically, the anisotropy parameter, plotted in Fig. 1(b), changes near eBE = 2.5 eV from positive values at lower binding energies to negative values at higher binding energies. In the simplest view, the anisotropy parameter depends on the electronic orbital from which photodetachment occurred. Therefore, a significant variation in β for different features in a photoelectron spectrum is often a signature of different neutral electronic states. Evidently, two different

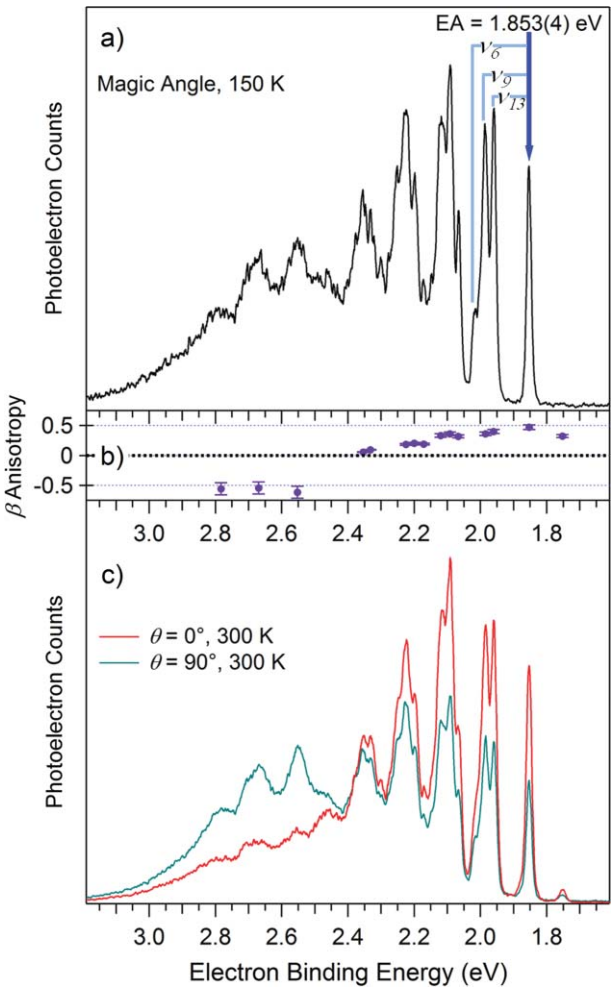

FIG. 1. (a) The 364-nm, magic angle, cold photoelectron spectrum of the furanide anion. The fundamental transitions of the ν_6, ν_9, and ν_{13} vibrational modes are marked. (b) β values of the major photoelectron peaks, indicating which features are due to the $\tilde{X}^2A'$ ground state ($\beta > 0$) and which are attributed to the $\tilde{A}^2A''$ excited state of α-furanyl radical ($\beta < 0$). (c) Spectra of the furanide anion, taken at 0° and 90° polarizations at room temperature and scaled to match the β anisotropy parameter of the origin peak (1.853 eV).

electronic states of neutral C_4H_3O are observed in the photoelectron spectra: the ground state at lower binding energy, and an excited state that appears at higher binding energy and is suppressed at $\theta = 0°$.

The electronic orbitals and valence electrons of α-furanide anion are presented in Fig. 2. Intuitively, we expect the ground state of the α-furanyl radical to result from the removal of an electron from the in-plane σ orbital of the deprotonated C_α, corresponding to a $^2A'$ σ-radical. Higher in

TABLE I. Measured and calculated (B3LYP/6–311++G(d,p)) electron affinities and term energies (T_e) of the α- and β-furanyl radicals.

		$\tilde{X}^2A' \leftarrow \tilde{X}^1A'$ (eV)	T_e (eV)
α-Furanyl radical	Experiment	1.853(4)	0.68(7)
	Theory	1.8866	0.6165
β-Furanyl radical	Experiment	...	...
	Theory	1.6712	1.0713

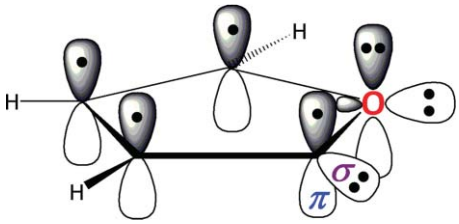

FIG. 2. Electronic orbitals and valence electrons of α-furanide, $\tilde{X}^1A'$. Photodetachment from the in-plane σ orbital of the deprotonated C_α yields the $\tilde{X}^2A'$ σ-radical ground state of the neutral furanyl radical. Photodetachment from the out-of-plane π cloud yields the $\tilde{A}^2A''$ π-radical excited state of the neutral furanyl radical.

energy lies the $^2A''$ π-radical resulting from the removal of an electron from the out-of-plane π orbital of a$''$ symmetry [see Fig. S1 (Ref. 48) for an illustration of the π molecular orbitals]. Between 0 and 3 eV of kinetic energy, "s-like" electrons give rise to $\beta > 0$ and "p-like" electrons yield $\beta < 0$. These labels reflect the character of the parent orbital: s-like electrons originate from orbitals with greater symmetry or fewer nodes than those that generate p-like electrons.[49] In other words, electrons removed from in-plane σ orbitals tend to have the greatest photodetachment cross sections parallel ($\theta = 0°$) to the laser polarization, whereas electrons in out-of-plane π orbitals have a maximum photodetachment cross section at $\theta = 90°$. As a result, positive β values are often associated with photoelectrons detached from in-plane orbitals of aromatic systems,[49–51] and negative β values are often found for photoelectrons detached from π orbitals of aromatic systems.[49,50,52,53] Thus, the positive β values observed at lower eBE in our spectra confirm that the lower energy vibrational progression corresponds to the $^2A'$ σ-radical ground state of the furanyl radical, i.e., the removal of an electron from the in-plane σ orbital of furanide. In contrast, $\beta < 0$ for the higher lying features because in this case the electron is detached from an out-of-plane π orbital. Furthermore, using the same simple picture, we can rule out the possibility that the two progressions represent the ground states of α- and β-furanyl radicals. Regardless of the deprotonation site, the ground-state furanyl radical is generated when an electron is removed from an in-plane σ orbital; thus, we expect $\beta > 0$ for the ground states of both α- and β-furanyl radicals.

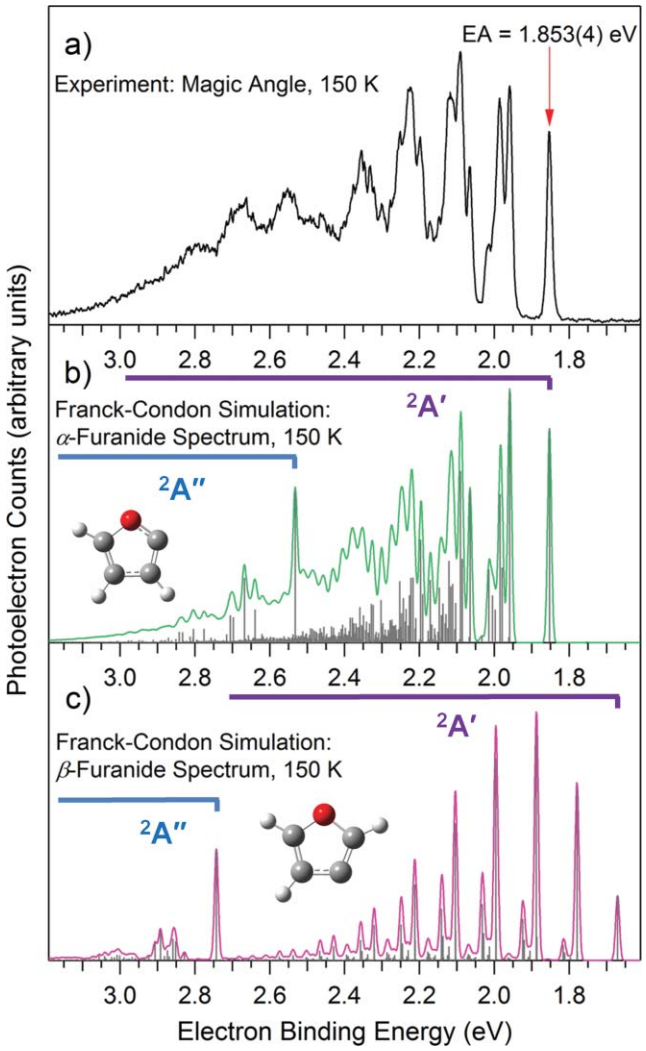

FIG. 3. (a) The 364-nm, magic angle, cold photoelectron spectrum of the furanide anion. (b) The simulated photoelectron spectrum of α-furanide anion. The simulation employs the experimentally measured EA (Table I) and the three experimental frequencies of the neutral (ν_6, ν_9, and ν_{13}) listed in Table III, determined from the comparison of the *ab initio* simulation to the experimental spectrum; we use calculated values for the remaining harmonic frequencies and all $\mathbf{K}''$ displacements (Table III). (c) The simulated photoelectron spectrum of β-furanide anion. The simulation uses *ab initio* EA, T_e, harmonic vibrational frequencies, and $\mathbf{K}''$ displacements, listed in Table I and Table S2. (b and c) The photoelectron signal due to the ground-state furanyl radical is marked with a purple bar, and the excited-state features are designated with a blue bar.

1. The $^2A'$ σ-radical ground state of the α-furanyl radical

Calculations and simulations of the photoelectron signal (plotted in Fig. 3) confirm our spectral assignments and enable a quantitative determination of several spectroscopic parameters. Table I lists the calculated and measured relative energies of the α- and β-furanyl species. The measured EA is in accord with the calculated origin of the α-furanyl radical. Figure 3(b) shows the Franck–Condon simulation of α-furanide photodetachment. The simulated $\tilde{X}^2A' \leftarrow \tilde{X}^1A'$ photoelectron spectrum, bracketed with a purple bar, reproduces the lower binding energy portion of the magic angle spectrum shown in Fig. 3(a). The agreement between the simulated and observed spectra further substantiates our assignment of the lower binding energy progression to the $\tilde{X}^2A'$ state of α-furanyl radical.

The relatively modest geometry change upon photodetachment implied by the well-resolved nature of the spectrum is supported by DFT calculations. Table II shows that detachment of an in-plane σ electron to generate the $\tilde{X}^2A'$ σ-radical distorts the ring to increase the O–•C–C angle about the radical center (•C) and shortens several bonds, especially the •C–C bond. Because the largest geometry change is the increase in the O–•C–C angle, the modes calculated to be most active in the Franck–Condon simulation are ν_{13} (a ring deformation mode dominated by the O–•C–C bend), ν_{12} (ring deformation that involves the C–C–C bend), and ν_9 (a ring breathing mode), illustrated in Fig. S2.[48] Franck–Condon

TABLE II. Optimized geometries of α-furanide anion ($\tilde{X}^1A'$) and α-furanyl radical ($\tilde{X}^2A'$, $\tilde{A}^2A''$), and the calculated net geometry change upon photodetachment (B3LYP/6–311++G(d,p)). Bond lengths are in units of angstrom (Å), and bond angles are in units of degree (°). The net geometry change is defined as the difference in the values of the internal coordinates for the anion and the radical. The bond lengths and angles that undergo the greatest change are boldfaced.

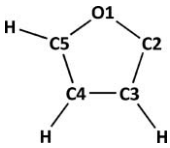

	α-Furanide	α-Furanyl radical		Geometry change	
Internal coordinate	$\tilde{X}^1A'$	$\tilde{X}^2A'$	$\tilde{A}^2A''$	$\tilde{X}^2A' \leftarrow \tilde{X}^1A'$	$\tilde{A}^2A'' \leftarrow \tilde{X}^1A'$
O1–C2	1.431	1.329	1.398	−0.012	**−0.033**
C2–C3	1.392	1.354	1.468	**−0.038**	**+0.076**
C3–C4	1.440	1.446	1.384	+0.006	**−0.056**
C4–C5	1.362	1.357	1.393	−0.005	**+0.031**
O1–C5	1.366	1.385	1.350	+0.019	−0.016
C3–H	1.084	1.076	1.080	−0.008	−0.004
C4–H	1.084	1.079	1.079	−0.005	−0.005
C5–H	1.082	1.076	1.081	−0.006	−0.001
∠O1–C2–C3	103.3	114.1	102.5	**+10.8**	−0.8
∠C2–C3–C4	110.9	103.4	110.7	**−7.5**	−0.2
∠C3–C4–C5	105.4	107.3	105.0	+1.9	−0.4
∠C4–C5–O1	109.9	109.6	110.9	−0.3	+1.0
∠C5–O1–C2	110.5	105.7	110.9	**−4.8**	+0.4

TABLE III. α-Furanide anion ($\tilde{X}^1A'$) and α-furanyl radical ($\tilde{X}^2A'$, $\tilde{A}^2A''$) vibrational frequencies. All but four of the frequencies listed in the table are unscaled calculated harmonic frequencies (B3LYP/6–311++G(d,p)). The ν_6, ν_9, and ν_{13} neutral frequencies and the ν_{13} anion frequency were determined from the Franck–Condon simulation of the $C_4H_3O^-$ photoelectron spectrum; these frequencies are listed in italics directly below the calculated value. The most active modes, based on the calculated geometry change and experimental peak intensities, are boldfaced.

				$\tilde{X}^2A' \leftarrow \tilde{X}^1A'$		$\tilde{A}^2A'' \leftarrow \tilde{X}^1A'$	
Mode		Description	Frequencies $\tilde{X}^1A'$ (cm^{-1})	**K″**	$\tilde{X}^2A'$ (cm^{-1})	**K″**	$\tilde{A}^2A''$ (cm^{-1})
A′	ν_1	C–H stretch	3202.5	−0.0055219	3288.8	−0.0039291	3248.8
	ν_2	C–H stretch	3172.9	−0.0043554	3274.1	−0.0053742	3232.4
	ν_3	C–H stretch	3157.6	1.7468×10^{-4}	3238.7	3.2151×10^{-4}	3224.8
	ν_4	C–C strech + H-wag	1537.2	−0.0096266	1568.1	0.013785	1400.0
	ν_5	C–C strech + H-wag	1369.2	−0.14452	1453.2	**0.16825**	**1096.9**
	ν_6	C–C strech + H-wag	1347.5	0.036363	1356.7	−0.016990	1475.3
					1307(40)[a]		
	ν_7	C–C strech + H-wag	1161.1	−0.011293	1229.9	**0.081375**	**1332.1**
	ν_8	H-wag	1105.5	0.079981	1167.5	−0.025052	1008.4
	ν_9	**C–O stretch**	**802.0**	**−0.18952**	**1093.7**	**−0.081214**	**718.6**
					1064(25)[a]		
	ν_{10}	C–O strech + H-wag	1072.6	−0.0067749	1019.9	−0.099751	1132.2
	ν_{11}	C–O strech + H-wag	982.1	0.036308	1000.3	0.068089	1029.0
	ν_{12}	**C–C–C bend**	**897.5**	**0.19493**	**875.0**	−0.062708	913.4
	ν_{13}	**O–C–C bend**	**852.0**	**0.35265**	**867.7**	**0.10232**	**865.5**
			815(30)[a]		***855(25)***[a]		
A″	ν_{14}	o–o–p H-wag	765.0	2.8862×10^{-5}	861.5	-5.9561×10^{-6}	919.4
	ν_{15}	o–o–p H-wag	740.8	2.4088×10^{-6}	777.3	8.1634×10^{-6}	813.8
	ν_{16}	o–o–p H-wag	628.2	-2.2699×10^{-6}	711.2	-1.6492×10^{-5}	901.7
	ν_{17}	o–o–p ring deformation	604.1	-9.2735×10^{-6}	602.3	2.3750×10^{-7}	499.8
	ν_{18}	o–o–p ring deformation	591.3	1.4156×10^{-6}	482.2	-3.7229×10^{-6}	699.9

[a] Experiment (this work).

activity of the various vibrational modes is indicated by their calculated $\mathbf{K}''$ displacements, which are vectors describing the difference in the nuclear equilibrium positions between the anion and the neutral radical. A large $\mathbf{K}''$ value indicates a vibrational normal mode vector that plays a large part in the net geometry change between the anion and the neutral. The calculated $\mathbf{K}''$ displacements are listed in Table III; as we intuitively expect, the largest $\mathbf{K}''$ displacements are for the ν_9, ν_{12}, and ν_{13} ring breathing and ring deformation modes.

The excellent agreement between the α-furanide $\tilde{X}^2\mathrm{A}' \leftarrow \tilde{X}^1\mathrm{A}'$ Franck–Condon simulation and the lower energy vibrational progression allows for partial characterization of the $\tilde{X}^2\mathrm{A}'$ state. Despite most peaks in the spectrum arising from multiple congested vibronic transitions [gray sticks in Fig. 3(b)], comparison of the *ab initio* simulation to the experimental spectrum enables us to assign features and measure vibrational frequencies based on photoelectron peaks dominated by a single vibronic transition. In this way, we extract three experimental vibrational frequencies of the ground-state radical (ν_6, ν_9, ν_{13}) and one experimental vibrational frequency of the anion (ν_{13}), which are listed along with the unscaled calculated frequencies in Table III. Though ν_6 is not one of the most active vibrational modes mentioned above, its fundamental transition is sufficiently well-resolved in the photoelectron spectrum to allow a confident determination of its frequency. The calculated and measured frequencies give rise to a simulated spectrum with peak positions that agree reasonably well with the observed vibrational structure. This is especially true at lower binding energy, which corresponds to the portion of the $\tilde{X}^2\mathrm{A}'$ potential energy surface where anharmonic effects are not significant. This suggests that the calculated harmonic vibrational frequencies accurately represent the vibrational frequencies of the $\tilde{X}^2\mathrm{A}'$ state of α-furanyl radical. In addition, the extent of the vibrational progression in the simulation, governed by the computed $\mathbf{K}''$ displacements (Table III), matches the observed spectral envelope. This agreement indicates that the calculated geometry change upon photodetachment is also consistent with the experimental spectrum.

2. The $^2A''$ π-radical excited state of the α-furanyl radical

We assign the higher energy vibrational progression to the $\tilde{A}^2\mathrm{A}''$ π-radical excited state of α-furanyl, in which an electron has been removed from the out-of-plane π molecular orbital of a″ symmetry [Fig. 2, Fig. S1 (Ref. 48)]. The Franck–Condon simulation of the excited state is bracketed in blue in Fig. 3(b). The origin transition of the $\tilde{A}^2\mathrm{A}''$ state of α-furanyl radical is predicted to be an intense peak at eBE = 2.5031 eV. The onset of the first intense feature for which $\beta < 0$, appearing at eBE = 2.53(7) eV, is assigned to the origin of the $\tilde{A}^2\mathrm{A}''$ state. Accordingly, its term energy is 0.68(7) eV, also in good agreement with the calculated T_e value. The ground-state α-furanyl radical lends some intensity to the photoelectron spectrum above 2.5 eV as well; there is an underlying unresolved continuum resulting from transitions to high vibrational levels of the $\tilde{X}^2\mathrm{A}'$ σ-radical. This continuum can be seen in the $\theta = 0^\circ$ spectrum [Fig. 1(c)], which minimizes contribution from the π-radical, and it is reproduced in the ground state Franck–Condon simulation.

The $\tilde{A}^2\mathrm{A}''$ features predicted by the Franck–Condon simulation appear in the experimental spectra, but are much broader than expected. Broad, diffuse spectral bands, such as those observed in the higher binding energy portion of the $C_4H_3O^-$ spectrum, are often characteristic of nonadiabatic effects.[54] Vibronic coupling between the $\tilde{X}^2\mathrm{A}'$ and $\tilde{A}^2\mathrm{A}''$ states of α-furanyl radical via their A″ vibrational modes can result in a large number of vibronic levels into which intensity can be distributed. The generally forbidden A″ modes of α-furanyl radical have frequencies between ~500 and 900 cm^{-1}; activity of these modes would fill in the excited state spectrum and broaden the resolved peaks predicted in the simulation by ~50 meV, which is consistent with the width of the peaks in the $\tilde{A}^2\mathrm{A}''$ progression. Such broadening of excited state features has also been observed in the photoelectron spectra of pyrrole (C_4H_5N) and thiophene (C_4H_4S),[55–58] as well as *N*-methyl-5-pyrazolide.[51] In all three cases, the width of the structure that could not be accounted for using Franck–Condon analysis[59,60] was attributed to vibronic coupling.[51,61]

We thus conclude that the higher binding energy vibrational progression in the $C_4H_3O^-$ magic angle spectrum is due to the $\tilde{A}^2\mathrm{A}''$ π-radical state of α-furanyl radical. The experimental T_e agrees well with calculations, and the discrepancy between the simulation and the observed spectrum is attributed to nonadiabatic effects.

3. Contribution from the β-furanyl radical

Calculations and Franck–Condon simulations of β-furanide photodetachment are shown in Fig. 3(c). Calculated equilibrium structures of the β-furanyl anion and radical states are given in Table S1; vibrational frequencies and $\mathbf{K}''$ displacements used in the simulation are listed in Table S2.[48] The simulation predicts a significantly more structured β-furanide photoelectron spectrum than the one observed experimentally, as well as a higher excited-state term energy, T_e ($\tilde{A}^2\mathrm{A}''$) = 1.07 eV. Even more importantly, the calculated EA of β-furanyl radical is 182 meV below that of the α-furanyl radical (Table I). We expect the calculated EA of β-furanyl radical to be reasonably reliable, as analogous calculations for the α-furanide species predict the EA to within 35 meV of the actual value. Likewise, the success of the Franck–Condon simulation of the α-furanide photoelectron spectrum lends credibility to the simulation of β-furanide. Thus, the discrepancies between the experimental $C_4H_3O^-$ spectrum and the calculated energy and vibrational structure of the β-furanide spectrum indicate that we do not observe significant signal from the β-furanyl radical under our experimental conditions. Furthermore, we observe no change in the relative intensity of features in the $C_4H_3O^-$ spectrum when experimental conditions are varied, which one might expect if signal from two different species were present in the photoelectron spectrum. Finally, as noted earlier, the negative β values above 2.5 eV binding energy rule out the possibility that the higher energy progression is due to the ground state of β-furanyl radical.

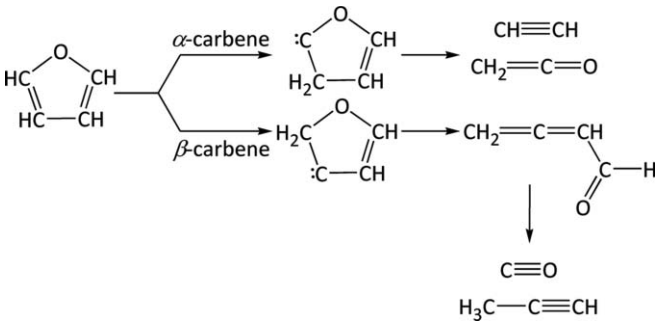

FIG. 4. Unimolecular decomposition pathways of furan.

B. C–H_α Bond dissociation energy of furan

One of the most significant results of this study is a direct measurement of the C–H_α BDE in order to evaluate the plausibility of various decomposition pathways of furan. The C–H_α BDE of furan, or $DH_{298}(C_4H_3O\text{-}H_\alpha)$, can be determined through the following thermochemical cycle:[32]

$$\begin{array}{rrll} & RH & \rightarrow R^- + H^+ & \Delta_{acid}H_{298}(C_4H_3O{-}H_\alpha) \\ & R^- & \rightarrow R + e^- & EA(\alpha - C_4H_3O) \\ + \; H^+ + e^- & & \rightarrow H & -IE(H) \\ \hline & & DH_{298}(RH) & DH_{298}(C_4H_3O{-}H_\alpha) \end{array} \quad (2)$$

The deprotonation enthalpy ($\Delta_{acid}H_{298}$) of furan was first reported in 1988 by DePuy *et al.*,[34] to be 388(3) kcal mol^{-1}, and more recently by Grabowski and Owusu[35] to be 390.7(2) kcal mol^{-1}. The ionization energy of hydrogen is well known: 313.6 kcal mol^{-1}.[33] Now, our measured value for the electron affinity of the α-furanyl radical [1.853(4) eV] enables the first experimental determination of the C–H_α BDE of furan: 119.8(2) kcal mol^{-1}.

In the currently accepted model of the unimolecular decomposition of furan, there are two fragmentation pathways that lead to the experimentally observed products, both of which involve H-rearrangement to a carbene intermediate as the initial step (Fig. 4).[1,29] In one pathway, an H_α migrates to the β-position of furan to form the α-carbene, which directly separates into HC≡CH + CH_2=C=O. Alternatively, an H_β can move to the α-position to form the β-carbene; further isomerization and decomposition of the β-carbene yields CO + $CH_3C{\equiv}CH$. The CH_2=C=CH–CHO intermediate could also lead to the formation of propargyl radical, CH_2=C=CH.[29] Our result for the C–H_α BDE substantiates the calculated value[1–3] and validates the accepted decomposition model of furan, in which C–H_α bond scission is prohibitively high in energy to be a viable route to furan decomposition.

This unusually high C–H_α BDE is more than 7 kcal mol^{-1} greater than the C–H BDE of the prototypical aromatic molecule benzene.[32] However, it is in accordance with other five-member heterocycles, which, like furan, have been shown to have very high C–H BDEs. For example, the C–H_α BDE of pyrrole (C_4H_5N) is 118(1) kcal mol^{-1}.[62] The C–H_α BDEs of the $C_3H_4N_2$ isomers imidazole[52] and pyrazole[50] are 119(4) and 121(4) kcal mol^{-1}, respectively. As in the case of the azoles, we attribute the high C–H_α BDE of furan to thermodynamic instability of the resulting radical. A computational study by Barckholtz *et al.* examined the effects of geometry and spin density on C–H BDEs of aromatic heterocycles[63] and concluded that the primary cause of the instability of the furanyl radical involves the localization of the unpaired electron. As a general rule, a radical is stabilized, thereby decreasing the C–H BDE, when its unpaired electron is delocalized over multiple atoms. In the case of furan, the unpaired electron of the α-furanyl radical is calculated to be almost completely localized on the $\bullet C_\alpha$. In fact, the excess spin density at the $\bullet C_\alpha$ radical center of furanyl radical is calculated to be slightly higher than the excess spin density at the radical center of phenyl radical, indicating that the extent of localization of the unpaired electron of the furanyl radical is slightly greater than that of the phenyl radical.[63] This effectively destabilizes the furanyl radical, leading to the high C–H_α BDE of furan.

V. CONCLUSION

We report the 364-nm photoelectron spectrum of the α-furanide anion. Two electronic states of the α-furanyl radical are observed. At lower binding energy, we find a well-resolved vibrational progression due to α-furanide $\tilde{X}^2A' \leftarrow \tilde{X}^1A'$ photodetachment. The adiabatic EA of the α-furanyl radical is determined to be 1.853(4) eV. Agreement between the $\tilde{X}^2A' \leftarrow \tilde{X}^1A'$ Franck–Condon simulation and the observed spectrum enables identification of several vibrational frequencies of the $\tilde{X}^2A'$ σ-radical ground state, given in Table III.

At higher binding energy, the photoelectron spectrum is dominated by photodetachment to the $\tilde{A}^2A''$ π-radical excited state of α-furanyl radical. The $\tilde{A}^2A''$ state lies 0.68(7) eV higher in energy than the $\tilde{X}^2A'$ state of the α-furanyl radical. The excited state signal is suppressed when the laser is polarized parallel to the direction of photoelectron collection ($\theta = 0°$). We see no evidence of C–H_β deprotonation, as Franck–Condon simulations for H_β removal have a significantly different structure and energy from the observed photoelectron spectrum.

Using the EA of α-furanyl radical measured in this work, together with the measured gas-phase acidity of furan[35] and the well-known ionization energy of H,[33] we determine the C–H_α BDE of furan to be 119.8(2) kcal mol^{-1} through a thermochemical cycle.[32] This experimental value is consistent with high-level calculations[1–3] that predict an exceptionally high C–H_α bond dissociation energy. The high C–H_α bond dissociation energy—7 kcal mol^{-1} greater than that of benzene[32]—can be attributed to thermodynamic instability of the resulting radical upon H_α loss.

ACKNOWLEDGMENTS

We are pleased to acknowledge generous support for this work from the US National Science Foundation and the US Air Force Office of Scientific Research. We are grateful to G. B. Ellison and A. Vasiliou for stimulating discussions, and to C. M. Chin for her advice and assistance in the preparation of deuterated samples. We also thank JILA Visiting Fellows D. L. Osborn and R. J. McMahon for sharing their insights on this topic.

[1]K. Sendt, G. B. Bacskay, and J. C. Mackie, J. Phys. Chem. A **104**, 1861 (2000).
[2]J. M. Simmie and H. J. Curran, J. Phys. Chem. A **113**, 5128 (2009).
[3]N. Sebbar, J. W. Bozzelli, and H. Bockhorn, Int. J. Chem. Kinet. **37**, 633 (2005).
[4]*The Structure and Reaction Processes of Coal*, edited by K. L. Smith, L. D. Smoot, T. H. Fletcher, and R. J. Pugmire (Plenum, New York, 1994).
[5]R. A. Meyers, *Coal Structure* (Academic, New York, 1982).
[6]J. Haggin, Chem. Eng. News **60**, 17 (1982).
[7]O. Beaumont, Wood and Fiber Science **17**, 228 (1985).
[8]J. Piskorz, D. Radlein, and D. S. Scott, J. Anal. Appl. Pyrolysis **9**, 121 (1986).
[9]R. J. Evans and T. A. Milne, Energy Fuels **1**, 123 (1987).
[10]R. J. Evans and T. A. Milne, Energy Fuels **1**, 311 (1987).
[11]F. Shafizadeh and Y. Z. Lai, J. Org. Chem. **37**, 278 (1972).
[12]F. Shafizadeh, G. D. McGinnis, and C. W. Philpot, Carbohydr. Res. **25**, 23 (1972).
[13]F. Shafizadeh, Y. Z. Lai, and C. R. McIntyre, J. Appl. Polym. Sci. **22**, 1183 (1978).
[14]S. Reale, A. Di Tullio, N. Spreti, and F. De Angelis, Mass Spectrom. Rev. **23**, 87 (2004).
[15]A. J. Ragauskas, C. K. Williams, B. H. Davison, G. Britovsek, J. Cairney, C. A. Eckert, W. J. Frederick, J. P. Hallett, D. J. Leak, C. L. Liotta, J. R. Mielenz, R. Murphy, R. Templer, and T. Tschaplinski, Science **311**, 484 (2006).
[16]S. Yaman, Energy Convers. Manage. **45**, 651 (2004).
[17]L. D. Gomez, C. G. Steele-King, and S. J. McQueen-Mason, New Phytol. **178**, 473 (2008).
[18]S. D. Phillips, Ind. Eng. Chem. Res. **46**, 8887 (2007).
[19]D. Fabbri, A. Adamiano, and C. Torri, Anal. Bioanal. Chem. **397**, 309 (2010).
[20]A. Oasmaa and D. Meier, J. Anal. Appl. Pyrolysis **73**, 323 (2005).
[21]H. Pakdel and C. Roy, Energy Fuels **5**, 427 (1991).
[22]P. A. Horne and P. T. Williams, Fuel **75**, 1051 (1996).
[23]A. Lifshitz, M. Bidani, and S. Bidani, J. Phys. Chem. **90**, 5373 (1986).
[24]P. P. Organ and J. C. Mackie, J. Chem. Soc., Faraday Trans. **87**, 815 (1991).
[25]D. Fulle, A. Dib, J. H. Kiefer, Q. Zhang, J. Yao, and R. D. Kern, J. Phys. Chem. A **102**, 7480 (1998).
[26]O. S. L. Bruinsma, P. J. J. Tromp, H. J. J. D. Nolting, and J. A. Moulijn, Fuel **67**, 334 (1988).
[27]M. A. Grela, V. T. Amorebieta, and A. J. Colussi, J. Phys. Chem. **89**, 38 (1985).
[28]N. R. Hore and D. K. Russell, New J. Chem. **28**, 606 (2004).
[29]A. Vasiliou, M. R. Nimlos, J. W. Daily, and G. B. Ellison, J. Phys. Chem. A **113**, 8540 (2009).
[30]E. B. Jochnowitz, X. Zhang, M. R. Nimlos, M. E. Varner, J. F. Stanton, and G. B. Ellison, J. Phys. Chem. A **109**, 3812 (2005).
[31]R. F. Liu, X. F. Zhou, and L. Zhai, J. Comput. Chem. **19**, 240 (1998).
[32]S. J. Blanksby and G. B. Ellison, Acc. Chem. Res. **36**, 255 (2003).
[33]S. G. Lias, "Ionization energy evaluations," in *NIST Chemistry WebBook, NIST Standard Reference Database Number 69*, edited by P. J. Linstrom and W. G. Mallard, National Institute of Standards and Technology, Gaithersburg, MD, http://webbook.nist.gov (retrieved August 5, 2010).
[34]C. H. Depuy, S. R. Kass, and G. P. Bean, J. Org. Chem. **53**, 4427 (1988).
[35]E. P. Clifford, P. G. Wenthold, W. C. Lineberger, G. B. Ellison, C. X. Wang, J. J. Grabowski, F. Vila, and K. D. Jordan, J. Chem. Soc., Perkin Trans. 2 **1998**, 1015 (1998).
[36]K. M. Ervin and W. C. Lineberger, in *Advances in Gas Phase Ion Chemistry*, edited by N. G. Adams and L. M. Babcock (JAI, Greenwich, 1992), vol. 1, p. 121.
[37]D. G. Leopold, K. K. Murray, A. E. S. Miller, and W. C. Lineberger, J. Chem. Phys. **83**, 4849 (1985).
[38]K. M. Ervin, J. Ho, and W. C. Lineberger, J. Chem. Phys. **91**, 5974 (1989).
[39]Y. L. Guo and J. J. Grabowski, Int. J. Mass Spectrom. Ion Process. **117**, 299 (1992).
[40]C. S. Feigerle, Ph.D. thesis, University of Colorado, 1983.
[41]D. M. Neumark, K. R. Lykke, T. Andersen, and W. C. Lineberger, Phys. Rev. A **32**, 1890 (1985).
[42]K. M. Ervin, W. Anusiewicz, P. Skurski, J. Simons, and W. C. Lineberger, J. Phys. Chem. A **107**, 8521 (2003).
[43]K. M. Ervin, PESCAL, Fortran Program (2010).
[44]J. Cooper and R. N. Zare, J. Chem. Phys. **48**, 942 (1968).
[45]M. J. Frisch, G. W. Trucks, H. B. Schlegel *et al.*, GAUSSIAN 03, Revision B.05. Gaussian, Inc., Pittsburgh, PA, 2003.
[46]R. Krishnan, J. S. Binkley, R. Seeger, and J. A. Pople, J. Chem. Phys. **72**, 650 (1980).
[47]K. M. Ervin, T. M. Ramond, G. E. Davico, R. L. Schwartz, S. M. Casey, and W. C. Lineberger, J. Phys. Chem. A **105**, 10822 (2001).
[48]See supplementary material at http://dx.doi.org/10.1063/1.3548873 for a table of the calculated equilibrium geometries of β-furanide and β-furanyl radical (Table S1), a table of calculated frequencies and K″displacements of the β-furanyl species (Table S2), a molecular orbital diagram of the excited state of α-furanyl radical (Fig. S1), and vector diagrams of the most active vibrational modes upon photodetachment (Fig. S2).
[49]R. F. Gunion, M. K. Gilles, M. L. Polak, and W. C. Lineberger, Int. J. Mass Spectrom. Ion Process. **117**, 601 (1992).
[50]A. J. Gianola, T. Ichino, S. Kato, V. M. Bierbaum, and W. C. Lineberger, J. Phys. Chem. A **110**, 8457 (2006).
[51]S. M. Villano, A. J. Gianola, N. Eyet, T. Ichino, S. Kato, V. M. Bierbaum, and W. C. Lineberger, J. Phys. Chem. A **111**, 8579 (2007).
[52]A. J. Gianola, T. Ichino, R. L. Hoenigman, S. Kato, V. M. Bierbaum, and W. C. Lineberger, J. Phys. Chem. A **109**, 11504 (2005).
[53]A. J. Gianola, T. Ichino, R. L. Hoenigman, S. Kato, V. M. Bierbaum, and W. C. Lineberger, J. Phys. Chem. A **108**, 10326 (2004).
[54]H. Koppel, W. Domcke, and L. S. Cederbaum, Adv. Chem. Phys. **57**, 59 (1984).
[55]P. J. Derrick, L. Asbrink, O. Edqvist, and E. Lindholm, Spectrochim. Acta A **27**, 2525 (1971).
[56]P. J. Derrick, L. Asbrink, O. Edqvist, B.-O. Jonssen, and E. Lindholm, Int. J. Mass Spectrom. Ion Phys. **6**, 161 (1971).
[57]P. J. Derrick, L. Asbrink, O. Edqvist, B.-O. Jonssen, and E. Lindholm, Int. J. Mass Spectrom. Ion Phys. **6**, 177 (1971).
[58]P. J. Derrick, L. Asbrink, O. Edqvist, B.-O. Jonssen, and E. Lindholm, Int. J. Mass Spectrom. Ion. Phys. **6**, 191 (1971).
[59]K. Takeshita and Y. Yamamoto, Chem. Phys. **189**, 489 (1994).
[60]K. Takeshita and Y. Yamamoto, J. Chem. Phys. **101**, 2198 (1994).
[61]A. B. Trofimov, H. Koppel, and J. Schirmer, J. Chem. Phys. **109**, 1025 (1998).
[62]J. C. Mackie, M. B. Colket, P. F. Nelson, and M. Esler, Int. J. Chem. Kinet. **23**, 733 (1991).
[63]C. Barckholtz, T. A. Barckholtz, and C. M. Hadad, J. Am. Chem. Soc. **121**, 491 (1999).